UC Irvine

UC Irvine Previously Published Works

Title

Monitoring conical intersections in the ring opening of furan by attosecond stimulated X-ray Raman spectroscopy

Permalink

https://escholarship.org/uc/item/8t85z2x6

Journal

Structural Dynamics, 3(2)

ISSN

2329-7778

Authors

Hua, Weijie
Oesterling, Sven
Biggs, Jason D
et al.

Publication Date

2016-03-01

DOI

10.1063/1.4933007

Peer reviewed

Monitoring conical intersections in the ring opening of furan by attosecond stimulated X-ray Raman spectroscopy

Weijie Hua,[1,a)] Sven Oesterling,[2,a)] Jason D. Biggs,[1] Yu Zhang,[1] Hideo Ando,[1] Regina de Vivie-Riedle,[2,b)] Benjamin P. Fingerhut,[1,3] and Shaul Mukamel[1,c)]

[1]*Department of Chemistry, University of California, Irvine, California 92697, USA*
[2]*Department of Chemistry, University of Munich, Butenandtstr. 5-13, D-81377 Munich, Germany*
[3]*Max-Born-Institut für Nichtlineare Optik und Kurzzeitspektroskopie, Max Born Strasse 2A, 12489 Berlin-Adlershof, Germany*

Attosecond X-ray pulses are short enough to capture snapshots of molecules undergoing nonadiabatic electron and nuclear dynamics at conical intersections (CoIns). We show that a stimulated Raman probe induced by a combination of an attosecond and a femtosecond pulse has a unique temporal and spectral resolution for probing the nonadiabatic dynamics and detecting the ultrafast ($\sim$4.5 fs) passage through a CoIn. This is demonstrated by a multiconfigurational self-consistent-field study of the dynamics and spectroscopy of the furan ring-opening reaction. Trajectories generated by surface hopping simulations were used to predict Attosecond Stimulated X-ray Raman Spectroscopy signals at reactant and product structures as well as representative snapshots along the conical intersection seam. The signals are highly sensitive to the changes in nonadiabatically coupled electronic structure and geometry. © *2015 Author(s). All article content, except where otherwise noted, is licensed under a Creative Commons Attribution 3.0 Unported License*. [http://dx.doi.org/10.1063/1.4933007]

I. INTRODUCTION

With the development of short femto- to picosecond light pulses,[1] it became possible to monitor molecular reactions in real time and determine ultrafast reaction rates.[2] Ultrafast photo-induced reactions are widely investigated in photochemistry and photobiology. Prominent examples are the photo damage and repair of the DNA bases,[3–6] the initial event in the process of vision,[7,8] electrocyclic photoreactions,[9–12] photodissociations,[13,14] and energy and charge transfer processes.[15] Ultrafast photodynamics is essential to current and emerging energy conversion and optical storage technologies. In many cases the observed dynamics can only be explained by the existence of conical intersections (CoIns)[16] a concept which has been established theoretically. CoIns are points where the molecule reaches a geometry for which potential energy surfaces of different electronic states come close in energy and may even become degenerate, and the Born-Oppenheimer (BO) approximation breaks down. The electronic and nuclear motions are strongly coupled and the molecule can rapidly relax nonradiatively to the lower lying electronic states, often all the way down to the ground state. A still existing caveat is that the rapid passage through a CoIn had so far prevented its direct spectroscopic observation. Only indirect evidence is available by recording the ultrafast changes in the spectroscopic signals of the reactants and the products in a pump-probe set up. CoIns lately became the focus of attention in the attosecond community.[17] Attosecond X-ray pulses have the capacity to probe

---

a)W. Hua and S. Oesterling contributed equally to the work.
b)Electronic mail: regina.de_vivie@cup.uni-muenchen.de
c)Electronic mail: smukamel@uci.edu

the ultrafast electron and nuclear dynamics through CoIn. Attosecond pulses are now produced by high harmonic tabletop sources,[18–21] and much brighter femtosecond X-ray pulses are made possible by free electron lasers.[22,23]

In this paper, we show how this may be accomplished by a novel spectroscopic detection scheme, Attosecond Stimulated X-ray Raman Spectroscopy (ASRS), depicted in Fig. 1. The molecule interacts with 3 pulses. The first UV actinic pulse, k_1, initiates the ring-opening reaction. After a time delay T, the molecule evolves to a superposition of valence states described by the density matrix $\rho_{ab}(T) = c_a c_b^*$. It then interacts with two X-ray pulses k_2 and k_3. The ~50 femtosecond Raman pump k_2 with frequency ω_2 is resonant with a core transition. The Raman probe k_3 is broadband (~100 attosecond) with mean frequency ω_3 red-shifted from ω_2. The Raman pump bandwidth is narrow compared with the lifetime broadening of the core transition and cannot induce an electronic Raman transition on its own. For example, a 30-fs pump has a FWHM bandwidth of 0.06 eV compared with the 0.13 eV lifetime broadening of the O1s core hole.[24] The signal is defined as the difference in the frequency dispersed transmission of the k_3 pulse with and without the Raman pump. This technique is commonly used in vibrational Raman spectroscopy, where it is known as femtosecond stimulated Raman spectroscopy (FSRS).[25–27]

We assume an oriented sample, with both pump and probe having the same polarization vector, ϵ. The transition dipole moments (TDMs) can then be replaced with their projection along this vector (that is, $V_{ij} = \boldsymbol{V}_{ij} \cdot \epsilon$). Assuming a monochromatic Raman pump $\mathcal{E}_2(\omega) = \delta(\omega - \omega_2)$, the ASRS signal is given by[28]
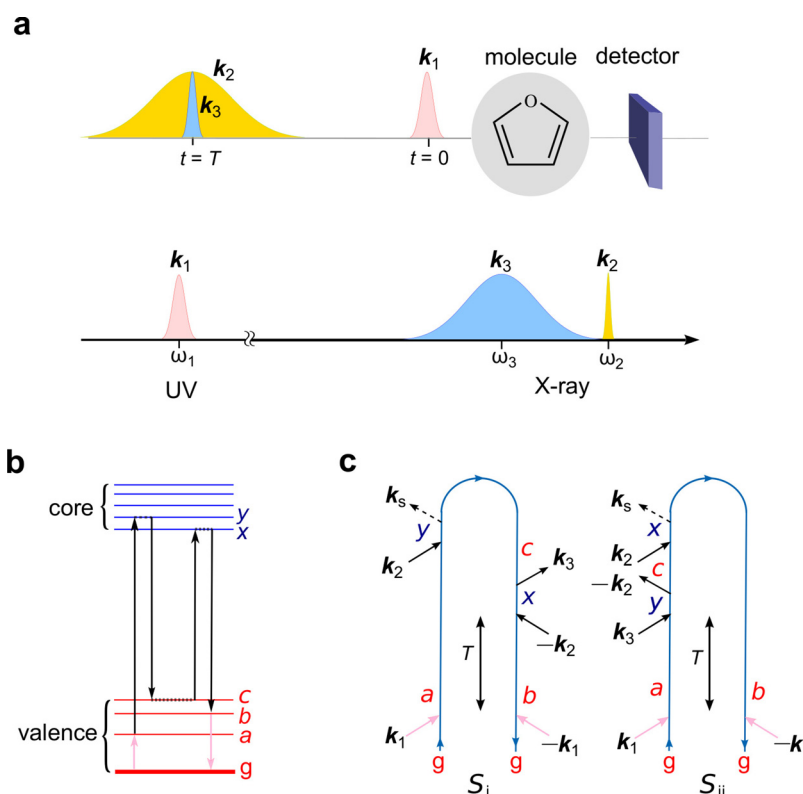

FIG. 1. Physical picture of the Attosecond Stimulated X-ray Raman Spectroscopy experiment. (a) Pulse sequence shown in the time (top) and frequency (bottom) domains. The UV actinic pump k_1 initiates the reaction, and after time delay T, the time coincident narrow femtosecond pump k_2 and broad attosecond probe X-ray pulses k_3 interact with molecule to generate the ASRS signal. (b) Energy level diagram and transition process involved in ASRS detection. State variables are according to Eqs. (2)–(3): a, b, c, valence-excited states (including the ground state g); x, y, core-excited states. Energy order in each manifold is arbitrary. (c) The two loop diagrams that contribute to the signal [Eq. (1)]. Both diagrams show a wavefunction evolution pathway along $b \leftarrow x \leftarrow c \leftarrow y \leftarrow a$, but vary in the interaction with the Raman sequence in either the bra or the ket side of the loop (see ref 66 for diagram rules).

$$S(\omega - \omega_2, \omega_2, T) = S_\text{i}(\omega - \omega_2, \omega_2, T) + S_\text{ii}(\omega - \omega_2, \omega_2, T), \qquad (1)$$

$$S_\text{i}(\omega - \omega_2, \omega_2, T) = -\text{Im} \sum_{abcxy} \frac{\rho_{ab}(T) V_{bx} V_{xc}^* V_{cy} V_{ya}^* \mathcal{E}_3(\omega) \mathcal{E}_3(\omega - \omega_{ab})}{(\omega_2 - \omega_{xb} - i\gamma_{xb})(\omega_2 - \omega_{ya} + i\gamma_{ya})(\omega - \omega_2 - \omega_{ac} + i\Gamma_{ac})}, \qquad (2)$$

$$S_\text{ii}(\omega - \omega_2, \omega_2, T) = \text{Im} \sum_{abcxy} \frac{\rho_{ab}(T) V_{bx} V_{xc}^* V_{cy} V_{ya}^* \mathcal{E}_3(\omega) \mathcal{E}_3(\omega - \omega_{ab})}{(\omega - \omega_{xb} + i\Gamma_{xb})(\omega - \omega_{yb} + i\Gamma_{yb})(\omega - \omega_2 - \omega_{cb} + i\Gamma_{cb})}. \qquad (3)$$

The two contributing terms S_i and S_ii can be, respectively, read off diagrams i and ii in Fig. 1(c). a, b, and c denote valence excited states (including the ground state), whereas x and y represent core-excited states, γ_α is the lifetime broadening of state α with $\Gamma_{\alpha\beta} = \gamma_\alpha + \gamma_\beta$, $\gamma_{\alpha\beta} = \gamma_\alpha - \gamma_\beta$, and $\omega_{\alpha\beta} = \omega_\alpha - \omega_\beta$ stands for the energy difference. $\mathcal{E}_3(\omega)$ is the Raman probe envelope. We also assumed that the electronic Hamiltonian does not change considerably during the fast interaction with the Raman probe (i.e., we neglect the dynamics during the interaction of the attosecond pulse). This is justified, since the X-ray Raman process occurs within the core lifetime ($\sim 5\,\text{fs}$),[29] whereby the nuclear motions are frozen. We watch the system valence dynamics by monitoring the signal variation with the time delay T.

We show that ASRS captures the geometrical and electronic structure changes when a CoIn is reached and passed, and can discriminate reactant, product, and CoIns with high sensitivity. This is confirmed by a complete active space self-consistent-field (CASSCF) spectroscopic study of the dynamics and relaxation pathways in the ring opening of photoexcited furan. Trajectories were generated by surface hopping nonadiabatic molecular dynamics (MD) simulations, and ASRS signals were calculated at selected snapshots.

II. RESULTS AND DISCUSSION

A. Passage through a conical intersection in a model system

The ultrafast passage through conical intersections is an example of a nonadiabatic transition—a fundamental problem in many chemical and biological systems.[30] The CoIn relaxation timescale and branching ratios are controlled by the topology of the branching space around the CoIn, the 2D subspace of nuclear degrees of freedom which lifts the degeneracy.[16] To set the stage for the ASRS signals of the nonadiabatic dynamics of a complex molecular system, i.e., the ring opening reaction of furan, we first illustrate the power of the technique with help of a simple model (see scheme in Fig. 2(e)) that captures the essentials of CoIn-mediated relaxation processes. 4 valence states, g (the ground state), e, e_2, and e_3, are coupled to 2 core excited states, f and f_2. A conical intersection is created by g and e. Starting from a bright e state, the dynamics is incorporated phenomenologically, by varying the energy gap between e and g (from $1\,\text{eV}$ to $0\,\text{eV}$ and back to $1\,\text{eV}$) as well as TDMs between g, e and core-excited states (all parameters provided in supplementary Note 1[31]).

The passage through a CoIn can in principle occur via three mechanisms. This is depicted in Figs. 2(a)–2(c) (left). Starting from a pure e state, states g and e switch state character (e.g., closed shell $\leftrightarrow \pi\pi^*$) after the passage. The passage can occur (i) via a diabatic mechanism, where the wavepacket relaxes to the ground state and keeps the state character, (ii) via an adiabatic mechanism, where the wavepacket stays in the excited state with the character interchanged, or (iii) via a branching mechanism which gradually mixes the former two.[32] Using the same set of energies and TDMs, different passing mechanisms are modeled by different time evolution of the quantum amplitudes (supplementary Fig. 1).

Figures 2(a)–2(c) (right) depict the simulated ASRS signals. Signal at the initial time ($T = -$) is the same for the three mechanisms. It is recaptured on top of Fig. 2(d) to demonstrate the ASRS peak features. Three major peaks contributed from diagram i (ii) are labeled by an A (1 and 2). For all these peaks, the same ASRS-active transition e $\leftarrow f_2 \leftarrow e_3 \leftarrow f_2 \leftarrow$ e (see Fig. 2(e)) is assigned, in the order of $b \leftarrow x \leftarrow c \leftarrow y \leftarrow a$. Resonances are generated when one or several factors in the denominator of Eqs. (2) and (3) vanishes: ω appears only
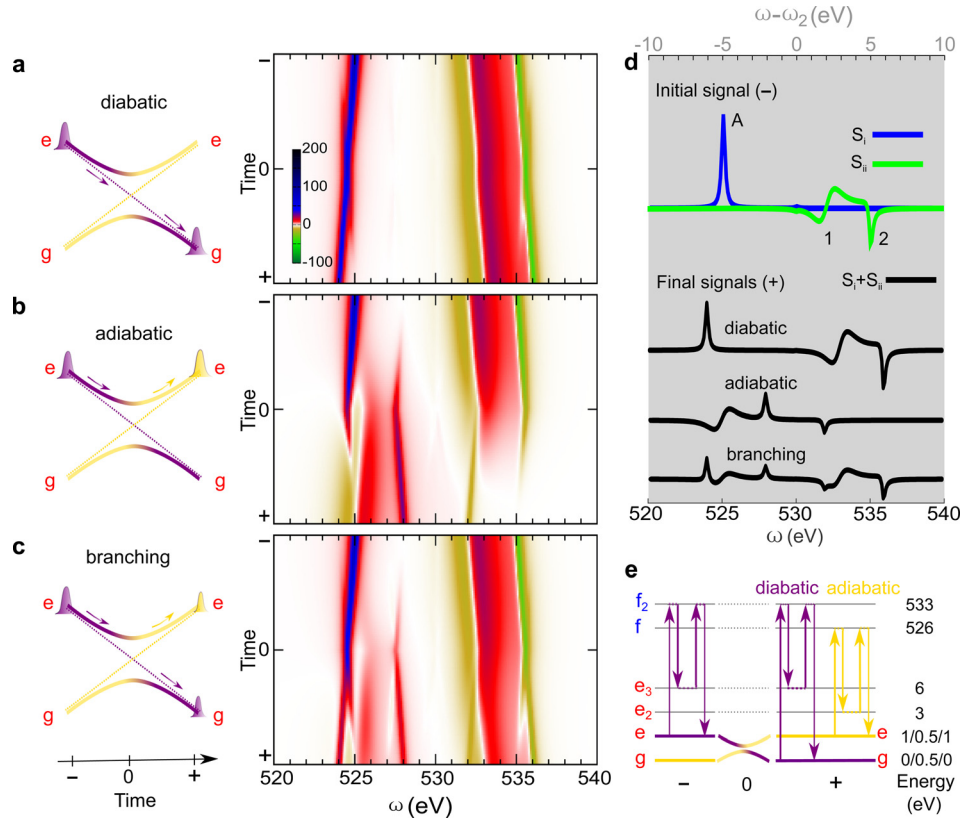
FIG. 2. Signals of a model system passing a conical intersection ($T = 0$) under 3 different mechanisms. (a)–(c) Left: Illustration of 3 mechanisms for passing a CoIn constituted by ground state g and valence excited state e, starting ($T = -$) from a wavepacket with only e populated, $|w_-\rangle = 1.0|e\rangle + 0|g\rangle$. States with different characters are colored by purple and gold, and arrows show the wavepacket evolution. Solid lines, adiabatic representation; dashes, diabatic representation. Right: 2D-plot of the simulated ASRS signals for the model system (defined in panel e) at different time under each mechanism. (a) Diabatic passage. The system relaxes to state g while the state character persists (purple line). We assume the system changes via $|w_0\rangle = \sqrt{0.5}|e\rangle + \sqrt{0.5}|g\rangle$ into $|w_+\rangle = 0|e\rangle + 1.0|g\rangle$ in our model. (b) Adiabatic process. The system remains in state e, but the state character changes. We set $|w_0\rangle = |w_+\rangle = |e\rangle = |w_-\rangle$. (c) Branching mechanism with partial population transfer. We adopt $|w_0\rangle = \sqrt{0.9}|e\rangle + \sqrt{0.1}|g\rangle$ and $|w_+\rangle = \sqrt{0.5}|e\rangle + \sqrt{0.5}|g\rangle$. (d) 1D slices of initial and final ASRS signals with respect to absolute (bottom axis) and relative (top axis) photon energies. Initial signal is decomposed as S_i and S_{ii}, and peaks are labeled. (e) Level scheme of the model of 4 valence and 2 core states. g and e have a switch in state character after the CoIn passage (purple and gold), and no change is assumed for other states (black). State energies are labeled. Only ω_e and ω_g vary during the process, to give a energy gap 1.0 eV at $T = -/+$ and 0.0 eV at $T = 0$. Additional parameters are given in supplementary Note 1. ASRS-active transitions at initial and final (diabatic and adiabatic passage) time are indicated by arrows.

once in S_i and resonances are attributed to $c \leftarrow a$ valence transition ($\omega - \omega_2 = \omega_{ac}$); ω appears three times in S_{ii}, indicating resonances to $b \leftarrow c$ valence transition ($\omega - \omega_2 = \omega_{cb}$), or $b \leftarrow y$ or $b \leftarrow x$ core deexcitation ($\omega = \omega_{yb}$ or $\omega = \omega_{xb}$). A single resonance from either diagram exhibits absorptive lineshape, and captures the valence transition information. The two absorptive peaks A and 2 correspond to the single valence resonance $e \leftarrow e_3$ and $e_3 \leftarrow e$, respectively. Their transition energies -5.0 eV and 5.0 eV can be read off the top axis (photon energy relative to ω_2). S_{ii} intensities can be greatly enhanced when two or three denominator factors approach zero at the same time (double- or triple-resonance), creating a dispersive-like lineshape. Among the multiple transitions, the double resonances for the same core transitions ($\omega = \omega_{xb} = \omega_{yb}$) are the easiest to be satisfied. The dispersive peaks are an effective probe for core transitions. Peak 1 corresponds to double resonances of the $e \leftarrow f_2$ core transition. The transition energy 532.0 eV (spreading 531.5–532.5 eV) can be read off the bottom axis (absolute photon energy). The dispersive peak magnitude depends on the core hole lifetime (supplementary Fig. 2).

Under the three mechanisms, signals evolve differently as different transitions are activated. For the diabatic passage (Fig. 2(a)), the involved state e is gradually transformed into g. At the final time ($T = +$), the active transition is g $\leftarrow$ f$_2$ $\leftarrow$ e$_3$ $\leftarrow$ f$_2$ $\leftarrow$ g (Fig. 2(e)). In the diabatic model, the ASRS signal provides a direct probe of the populated state character irrespective of the energy order. The energy order switch leads to a red shift of peak A and a blue shift of peaks 1 and 2 by 1.0 eV ($= \omega_{eg}$). Clear signal changes are observed during the adiabatic passage (Fig. 2(b)). This is because a different type of transition e $\leftarrow$ f $\leftarrow$ e$_2$ $\leftarrow$ f $\leftarrow$ e (Fig. 2(e)) is probed as time goes (while contribution of the initial transition channel decays) and uniquely remains till the end. Two absorptive peaks at $\omega - \omega_2 = -2.0, 2.0$ eV from S_i and S_{ii} probe single valence resonance e $\leftarrow$ e$_2$ and e$_2$ $\leftarrow$ e, respectively. A dispersive S_{ii} peak at $\omega = 525.0$ eV (spreading 524.5–525.5 eV) probes the double core resonance e $\leftarrow$ f. In the 2D signal of Fig. 2(b), these new peaks become gradually stronger, and the S_i and S_{ii} peaks manifest blue and red shifts. Figure 2(c) gives the signals of a prototypic population branching mechanism. Significant signal changes are observed during the passage, which arise from the adiabatic pathway. At the final time, the system is still in a superposition of states e and g (supplementary Fig. 1(c)), and the final signal combines features of the former two mechanistic limiting cases (Fig. 2(d)).

B. Semiclassical molecular dynamics simulations of furan

Nonadiabatic MD simulations of the relaxation of photo-excited furan were performed using Tully's fewest switch trajectory surface hopping (TSH) algorithm.[33] 100 250-fs trajectories were generated where 4 low-lying singlet valence states (S$_0$–S$_3$) were considered at the state-averaged CASSCF level. The simulations started with a bright $\pi\pi^*$ state S$_2$ prepared by the actinic pump and shortly underwent a population redistribution to S$_1$ (supplementary Fig. 3). Then in an average time of 95 fs, S$_1$/S$_0$ CoIn structures were reached with smooth variation from deformed to ring opening geometries. Most trajectories ended in the ground state S$_0$, in agreement with previous predictions.[34] Both pathways, the deformation,[35] as well as relaxations through a ring opening, were observed.

Snapshots were selected, aiming to study the signal change (1) among the reactant, S$_1$/S$_0$ conical intersection, and product; and (2) during the diabatic/adiabatic passage of the CoIn. The conical intersections are not isolated points but form multidimensional seams. Signals for several CoIns within the seam are compared in supplementary Fig. 13. Nuclear coordinates and amplitudes of electronic states were used for the ASRS signal calculations. We had increased the number of states (from 4 S$_0$–S$_3$ to 10 V$_0$–V$_9$) and basis set (6-31G* to aug-cc-pVDZ) to achieve more accurate and broad signals. The amplitudes of S$_0$–S$_3$ were projected into the new basis set, and the original S$_1$/S$_0$ CoIn can be tracked as the V$_1$/V$_0$ CoIn (supplementary Note 2).

C. Signals at the reactant, conical intersection, and product configurations

To observe the structural changes around the C–O bond in the ring opening reaction, we focused on the core excitations at the O1s edge. This avoids the complexity caused by multiple core centers at the C1s edge.[36] 50 core excited states (C$_1$–C$_{50}$) were computed with the state-averaged restricted-active-space SCF (RASSCF) method.[37] The Raman pump frequency was set to 533.0 eV. A Gaussian spectral envelope $\mathcal{E}_3(\omega) = e^{-\sigma^2(\omega-\omega_3)^2/2}$ was used for the broadband probe pulse, with ω_3 set to 528.0 eV and pulse duration $\sigma = 100$ as. Most trajectories followed the ring opening pathway, where a possible product is a 3-membered ring. We picked one trajectory, traj. 3, which ran into a comparable geometry, and selected 3 snapshots at $T = 0.0$ fs (**Reac-3**), 62.5 fs (**CoIn-3**), and 231.0 fs (**Prod-3**) as representative structures for the reactant, conical intersection, and product (see structures in Fig. 3(c)). The resulting ASRS signals displayed in Fig. 3(a) reveal strong variations in both shapes and magnitudes. This is to be expected due to the drastic changes in geometry and electronic structure. Absolute magnitude of the signals are sensitive to transition dipole moments due to the quadratic dependence [Eqs. (2) and (3)]. Here, **Reac-3** has absolute intensity 10^3 orders lower than the others simply
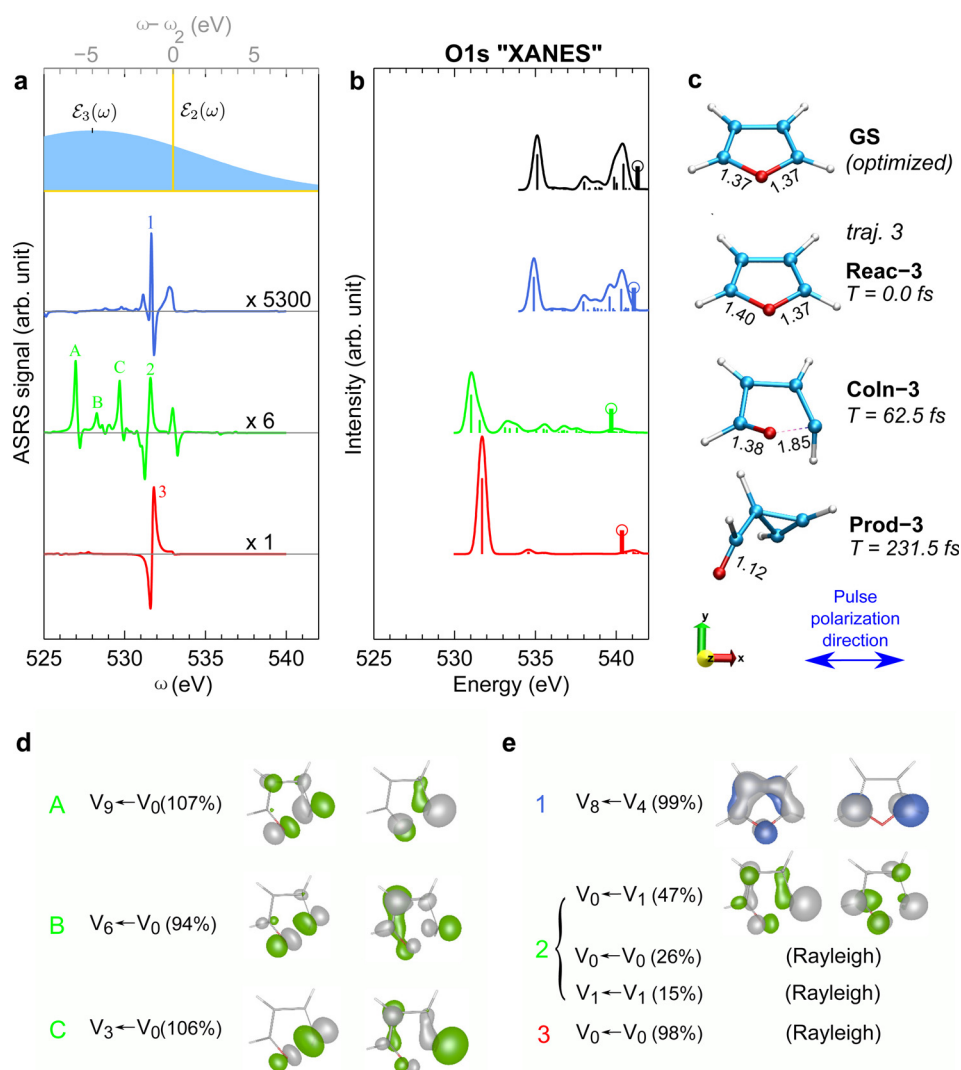
FIG. 3. Signals for reactant, conical intersection, and product geometries. (a) Simulated O1s ASRS signals of furan at 3 snapshots along trajectory 3: reactant **Reac-3**, conical intersection **CoIn-3**, and product **Prod-3**. Intense peaks contributed by diagrams i (ii) are labeled by A (1 and 2). Envelopes of pulses 2 and 3 ($\mathcal{E}_2$ and $\mathcal{E}_3$) are shown on the top. (b) Simulated artificial "O1s XANES spectra" at these snapshots and the optimized ground-state geometry. Stems label calculated O1s IPs. (c) Corresponding geometries, with C–O distances given in Å. (d) Assignment of major transitions. Percentages in parenthesis are contributions of the specified major transitions divided by S_i or S_{ii}. (e) Raman transitions are analyzed in terms of the natural transition orbitals (NTOs),[38–40] where dominant particle (left) and hole (right) orbital pairs are plotted with contour isovalue = 0.08.

because small X component of TDM between active valence and core states (it is a nearly planar structure put in the XY plane and we set the photon X-polarized).

The dominant peaks from diagram i (ii) are labeled by A, B, C (1, 2, 3). Separate plots of S_i and S_{ii} contributions are provided in supplementary Fig. 4; experimentally, we only observe their sum. Peaks assignments are given in Table I. Peak 1 of **Reac-3** is interpreted as $V_8 \leftarrow C_{23} \leftarrow V_4 \leftarrow C_{23} \leftarrow V_8$. Triple resonances lead to a strong dispersive peak. Valence transition frequency $\omega(V_4) - \omega(V_8) = -1.4$ eV and core transition frequency $\omega(C_{23}) - \omega(V_8) = 531.7$ eV can be directly read from the top and bottom axes, respectively. Peak 3 of **Prod-3** probes double resonances for the core transitions $V_0 \leftarrow C_1$. Mixing of different channels appears in **CoIn-3**. The impurity is caused by the two constituting states V_0 and V_1 (projected

TABLE I. ASRS peak assignments. Assignments of major transitions along the entire pathway of wavefunction evolution $b \leftarrow x \leftarrow c \leftarrow y \leftarrow a$ (Fig. 1(c)) for ASRS peaks defined in Fig. 3(a). Peak positions are in eV.

Geometry	peak	position	$b \leftarrow x \leftarrow c \leftarrow y \leftarrow a$
Reac-3	1	531.7	$V_8 \leftarrow C_{23} \leftarrow V_4 \leftarrow C_{23} \leftarrow V_8$
CoIn-3	A	527.0	$V_{0,1} \leftarrow C_{3,4,2} \leftarrow V_9 \leftarrow C_{3,4,2} \leftarrow V_0$
	B	528.3	$V_{0,1} \leftarrow C_{3,4,2} \leftarrow V_6 \leftarrow C_{3,4,2} \leftarrow V_0$
	C	529.7	$V_{0,1} \leftarrow C_{3,4} \leftarrow V_3 \leftarrow C_{3,4} \leftarrow V_0$
	2	531.6	$V_{0,1} \leftarrow C_2 \leftarrow V_{1,0} \leftarrow C_2 \leftarrow V_{1,0}$
Prod-3	3	531.8	$V_0 \leftarrow C_1 \leftarrow V_0 \leftarrow C_1 \leftarrow V_0$

from S_0 and S_1; supplementary Note 2), which have close energy (ca. 0.1 eV) and similar state population. For instance, peak 2 (from S_{ii}) is interpreted as $V_{0,1} \leftarrow C_2 \leftarrow V_{1,0} \leftarrow C_2 \leftarrow V_{1,0}$. To see the involved valence transitions between the two states, we decomposed the signal into each (b, c) pair as the S_{ii} channel probes the $b \leftarrow c$ valence transition. This assigns a mixture of anti-Stokes transition $V_0 \leftarrow V_1$ (47%) and Rayleigh transitions $V_0 \leftarrow V_0$ (26%) and $V_1 \leftarrow V_1$ (15%).

We had further analyzed the valence Raman transitions in terms of the natural transition orbitals (NTOs)[38–40] (Figs. 3(d) and 3(e)). The NTOs obtained from singular value decomposition of the spin-summed transition density matrix provide a visual illustration of each transition through one or several hole and particle orbitals (NTO pairs). For instance, the $V_8 \leftarrow V_4$ to transition of **Reac-3** (peak 1) is mainly characterized by the creation of an electron in the delocalized, bonding π orbital and a hole in the localized, anti-bonding C-p_z orbitals. **CoIn-3** is a biradical. Peak A is characterized as $V_9 \leftarrow V_0$ transition, through which the biradicals on the two terminals become more delocalized. By contrast, in peaks B and C, the electrons are transferred from a delocalized π orbital to be more localized on the two terminals. For peak 2, the NTOs picture the electron movement for the $V_0 \leftarrow V_1$ transition.

Figure 3(b) gives the simulated O1s X-ray absorption near edge structure (XANES) spectra from the ground state at each geometry. Even though these are not experimental observables (since the molecule is in a superposition of valence states instead of ground state), they provide a window into the transition energies and dipole moments. In **CoIn-3** and **Prod-3**, the C–O bond is broken and the oxygen site becomes a radical. This leads to a 3–4 eV red shift for the main peak positions in the simulated XANES spectra, as compared to **GS** or **Reac-3**. A similar red shift was observed experimentally in the C1s XANES spectra of the $\cdot$ CH$_3$ radical.[41] Unlike XANES, there is no large global shift in the ASRS signals because the broadband pulse covers a wide region (ca. 10 eV, top of Fig. 3(a)) and can excite different valence-core transitions.

D. Signals in the vicinity of conical intersections

The ASRS signals clearly reveal the rapid passage through a CoIn. We use two MD trajectories 21 and 24 to illustrate the diabatic and adiabatic passage, respectively. Figure 4 displays the energy and amplitude variation of four states S_0–S_3 in the first 50 fs of the MD simulations. Initially, the molecule is excited to the bright S_2 state, then it redistributes into S_1 during 15.0–25.0 fs, reaching the S_1/S_0 CoIn at 29.0 fs (traj. 21) or 28.5 fs (traj. 24). The difference is that the system then turns into S_0 in traj. 21, while it remains in S_1 in traj. 24. The two constituting states populations change steeply in the vicinity of a CoIn. We study the passage for 10 consecutive snapshots in a time window of 4.5 fs (26.5–31.0 fs). Each set provides a series with minor perturbations in chemical structure but show noticeable variations in electronic structure due to the breakdown of the BO approximation.

Figure 5(a) displays the simulated ASRS signals of traj. 21, where from left to right we show the total signal and separated contributions arising from populations (ρ_{00} and ρ_{11}) and the coherence ($\rho_{01} + \rho_{10}$) of the two constituting states, V_0 and V_1. The system gradually evolves from V_1 to V_0 (see their amplitudes in Fig. 5(b); other valence states have negligible
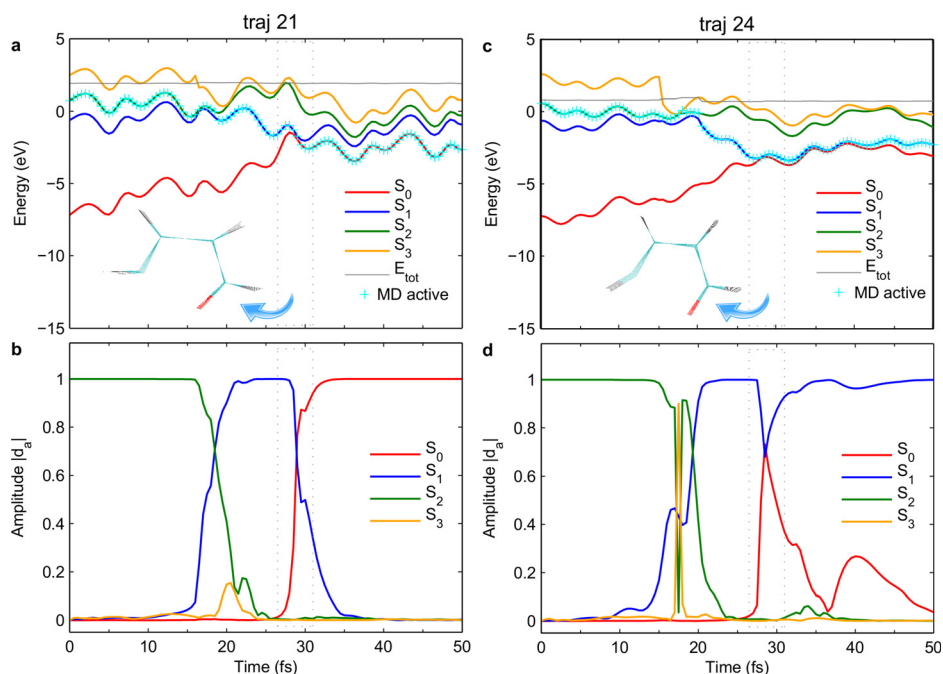
FIG. 4. Time-dependent energies and amplitudes. Time-dependent CASSCF energies (top) and amplitudes (bottom) of valences states S_0–S_3 in the first 50 fs of (a) and (b) MD traj. 21 and (c) and (d) traj. 24. The S_1/S_0 CoIn of the two trajectories appears at ca. 29.0 fs and 28.5 fs and is characterized as mainly diabatic and adiabatic passage, respectively. A time window of 4.5 fs ($T = 26.5$–31.0 fs, see dotted boxes) is chosen to study its CoIn passage (enlarged view provided in supplementary Fig. 5). Insets show the superposition of snapshots in the time window, with rmsd change in coordinates of 0.11 and 0.18 Å, respectively. In top panels, cyan crosses denote MD-active states and gray lines are total energies (sum of kinetic and potential energies).

amplitudes, see supplementary Note Fig. 2). The total signal is thus dominated by the ρ_{11} component first and then by ρ_{00}. In the middle region ($T = 28.5$–29.5 fs), both states have comparable populations (thus induce coherence of comparable magnitude), so the total signal is composed by both population and coherence terms on similar footing. Time-dependent signals exhibit a "jump" around 29.0 fs (see also 2D contour plot in supplementary Fig. 6), which reflect the geometry and electronic structure changes in furan when the CoIn is approached. Such signal variation is caused by the change in valence-core transition dipole moments, and the sensitivity comes from the quadratic dependence which amplifies the difference. The evolution of V_0-core and V_1-core TDMs is interpreted in supplementary Fig. 7 by using the corresponding Gaussian convoluted oscillator strengths, where each exhibits a piecewise function switching at 29.0 fs. Apart from the short transition period (say, before 28.0 fs and after 29.5 fs), the electronic structure evolves much more slowly and accordingly the signals show relatively mild changes.

To understand the signal evolution, coherence contributions, and resonances that enhance the signals during the CoIn, we followed a major absorptive peak at ca. 527 eV (labeled by "o"), which comes from the S_i channel. The peak is interpreted as $V_1 \leftarrow C_3 \leftarrow V_9 \leftarrow C_3 \leftarrow V_1$ in the beginning (till 28.0 fs), and $V_0 \leftarrow C_3 \leftarrow V_9 \leftarrow C_3 \leftarrow V_0$ in the end (from 29.5 fs). While in the transition period (28.5–29.0 fs), both V_0 and V_1 are involved. The switch from V_1 to V_0 involved in the major transitions indicates that the ASRS signal picks up the state features regardless of their energy reversal. Underlying valence transitions ($V_9 \leftarrow V_1$ or $V_9 \leftarrow V_0$) are interpreted as mainly oxygen p orbital to π^* transitions by the NTOs (Fig. 5(c)). The NTOs verify the similar features of active transitions during the time. Meanwhile, they also visualize the progression for these transitions. As time increases, the hole (particle) orbitals change from delocalized to localized on the O atom (C-O terminals).

The calculated ASRS signals of traj. 24 is given in Fig. 6(a) to demonstrate the signal evolution during the adiabatic passage of the V_1/V_0 CoIn. The CoIn is approached at ca. 28.5 fs.
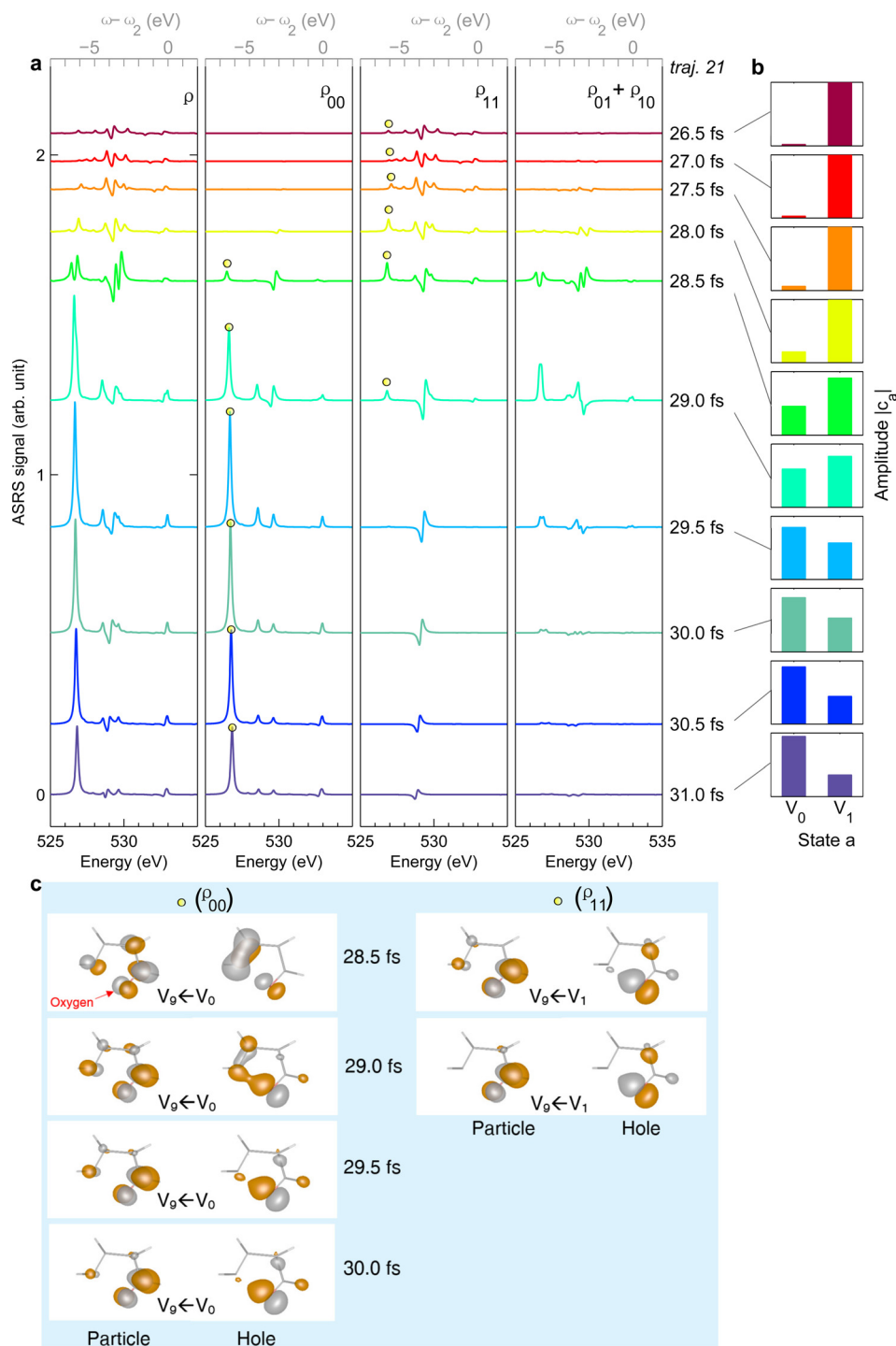
FIG. 5. Rapid variation of ASRS signals in diabatic passage of a conical intersection. (a) Simulated ASRS signals of furan during the diabatic passage of V_1/V_0 conical intersection ($T = 26.5 - 31.0$ fs in MD trajectory 21). From left to right, total signals and contributions from ρ_{00} and ρ_{11} populations, and $\rho_{01} + \rho_{10}$ coherence (0 and 1 refer to states V_0 and V_1). (b) Absolute amplitudes of the two constituting states. (c) Major valence transitions (denoted by "o") visualized by NTOs at selected time. Dominant hole and particle orbitals are plotted with contour isovalue = 0.08.

The wavepacket still remains in state V_1 after passing the CoIn (in contrast to traj. 21; Fig. 6(b)), while the state character of V_1 and V_0 interchanges. As a result of the evident total signal change around the transition point (cf. signals at 27.5 – 29.0 fs in Fig. 6(a); see also 2D plot in
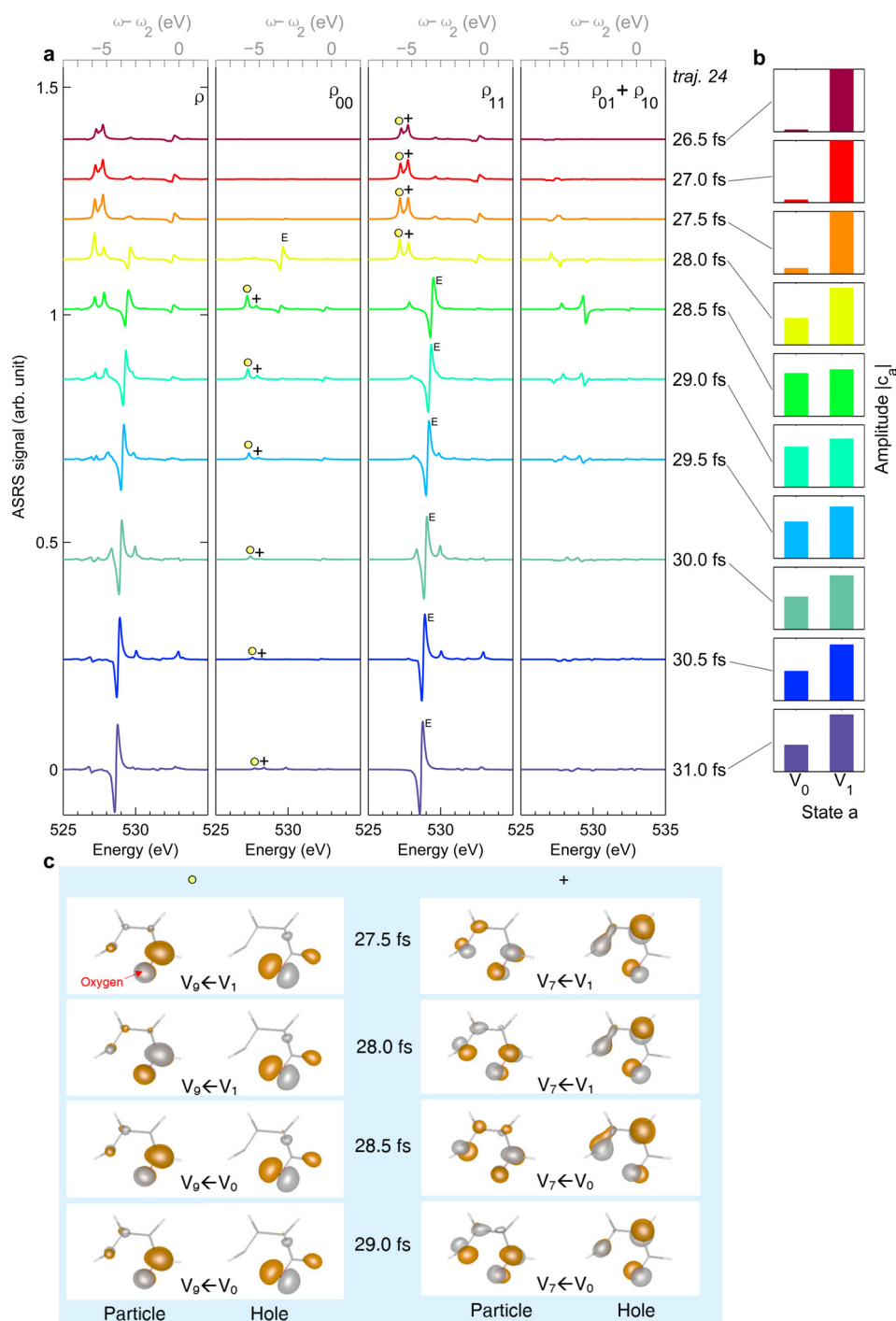
FIG. 6. Rapid variation of ASRS signals in adiabatic passage of a conical intersection. (a) Simulated ASRS signals of furan during the adiabatic passage of V_1/V_0 conical intersection ($T = 26.5 - 31.0$ fs in MD trajectory 24). From left to right, total signals and contributions from ρ_{00} and ρ_{11} populations, and $\rho_{01} + \rho_{10}$ coherence (0 and 1 refer to states V_0 and V_1). (b) Absolute amplitudes of the two constituting states. (c) Major valence transitions for the two main peaks (denoted by "+" and "o") visualized by NTOs at selected time. Dominant hole and particle orbitals are plotted with contour isovalue = 0.08.

supplementary Fig. 8), the absorptive double peaks at 527–528 eV (denoted by "o" and "+") decay while the dispersive, elastic peak (denoted by "E") at 528.5 eV grows. For instance, peak "o" comes from $V_1 \leftarrow C_{2,3} \leftarrow V_9 \leftarrow C_{2,3} \leftarrow V_1$ in the beginning and $V_0 \leftarrow C_{2,3} \leftarrow V_9 \leftarrow C_{2,3} \leftarrow V_0$ transitions in the end. Clear sequence and progression of the NTOs for valence

Raman transitions is depicted in Fig. 6(c). The peak E corresponds to elastic valence transition $V_0 \leftarrow V_0$ transition at 28.0 fs and $V_1 \leftarrow V_1$ since 28.5 fs, both via an intermediate core state C_1. The evolution of V_0-core and V_1-core TDMs is interpreted in supplementary Fig. 9.

E. Ensemble averaging

Above discussion had shown that the ASRS signals are capable to probe the diabatic or adiabatic passage of a CoIn along an individual trajectory. Experiments however record the ensemble average of many trajectories which may average out some features. Ensemble averaging over the complete trajectory evolution would require repeating the whole computational procedure for hundreds (more likely thousands) of trajectories, which is computationally extremely expensive. We focus on the fast appearance (< 40 fs) of the S_1/S_0 CoIns of the ring opening pathway. Within the short period, the trajectories sample a limited phase space and approximately resemble a compact wavepacket. We performed 300 short 40 fs MD simulations (in addition to the 100 250 fs MD trajectories), and chose the sub-ensemble of trajectories approaching the CoIn between 26.5–31.0 fs (most trajectories did not approach the S_1/S_0 CoIn within the period). ASRS signals are then evaluated within this narrow time window to obtain good statistics. Totally 15 trajectories (including trajs. 21 and 24) were selected out (see structures in supplementary Fig. 10), and the signal evolution of each trajectory was calculated. For most trajectories, the initial wavepacket at 26.5 fs has a dominant S_1 population and mainly $\pi\sigma^*$ character. They constitute a rich set for the evolution of amplitudes ($S_0 \leftarrow S_1$) and character $[\pi^2 \leftarrow (\pi)^1(\sigma^*)^1]$ to different extent (i.e., including those mainly retain the character). They show how the signals overlap and how the branching of different pathways would be observed. It has been shown above that when the electronic structure change is mild, the signal progression is slowed down. It is therefore reasonable to assume that the omitted trajectories contribute a smooth background within this time window.

Figure 7 displays the simulated averaged signal. It exhibits two clear regions contributed mainly from S_i and S_{ii}, respectively, and include two absorptive (labeled by "o" and "*") and one dispersive major features ("E"). Features of individual features can still be recognized. One important reason is that absolute signal intensity of individual trajectory varies by orders of 1–100 (due to the sensitivity to the TDMs). For instance, traj. 21 contributes to the feature "o" starting at 29.0 fs, while traj. 24 makes invisible contribution (cf. intensity scales in supplementary Figs. 6 and 8). Statistics selects out those trajectories with strong intensities, with limited smearing effect by others. Additional feature "*" in the S_i region comes from the $V_8 \leftarrow V_1$
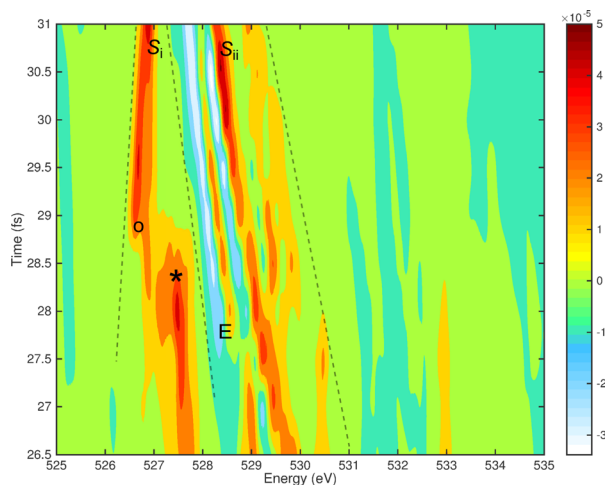

FIG. 7. Statistical average. Two-dimensional plot of the simulated ASRS signals averaged over 15 trajectories during the period 26.5–31.0 fs. The signals feature two evident regions (dashes are added to guide eyes), which mainly come from the S_i and S_{ii} channels, respectively. Three peak features are labeled as "o," "*" (absorptive peaks) and "E" (dispersive peak) at where they appear or disappear.

transition which starts to disappear at around 28.5 fs, indicating a CoIn at this region (see a constituting trajectory contribution in supplementary Fig. 11). Thus, the ASRS technique has its own capacity to record the main feature and turning point of different channels according to their signal intensities. Those with large absolute intensities are highly visible in the averaged signal. The S_{ii} region exhibits evident red shift. A dispersive feature "E" appears at around 27.5 fs and then gradually increases in intensity. It corresponds to mainly $V_1 \leftarrow V_1$ (and slightly $V_0 \leftarrow V_0$) elastic transition and appears in many trajectories (see a contributing trajectory in supplementary Fig. 12). Since this peak resonates with the state with π^2 character, the increase in intensity qualitatively refers to the yield via the adiabatic passage. Thus, it indicates branching of different trajectories between the adiabatic and diabatic relaxation channels upon passage of the CoIn. The ASRS technique provides the required selectivity to record the distinct relaxation channels which arise from non Born-Oppenheimer branching events in the vicinity of CoIn.

III. CONCLUSIONS

ASRS signals of photo-excited furan simulated at the CASSCF level reveal microscopic details of the ring-opening pathways. ASRS is highly sensitive to the electronic structure and serves as a probe for its variation during ultrafast reactions. The signals calculated for representative snapshots provide clear signatures which allow to discriminate reactant, product, and transient conical intersection structures as well as different CoIn structures in the seam (supplementary Fig. 13). Furthermore, the nonadiabatic transitions in the vicinity of conical intersections can be resolved by the proposed technique. Underlying physical processes of major ASRS peaks have been analyzed in detail. Absorptive and dispersive peaks have been interpreted: mathematically, they come from the single- and multiple- (double and triple) resonances, respectively, and chemically, they map out the valence and core resonance information, respectively.

In the ASRS technique, the attosecond pulse serves as a sharp time mark and ruler to accurately measure the time delay T to the actinic pump—by scanning T, the system dynamics can be monitored. Attosecond pulses have a broadband spectrum. For example, pulse duration of 100 attoseconds cover an energy range of 10–20 eV. This offers a broader window into electronic valence transitions. It is thus capable to follow the entire valence state evolution regardless of changing inter-valence transition moments or vanishing energy gap during the valence state relaxation dynamics. Attosecond pulses can be generated in the X-ray or XUV regime. When the carrier frequency falls in the X-ray regime, the spectroscopy is element-specific. By tuning the pulse frequency to excite the atom that is directly involved in the bond breaking, the chemical structure change during the reaction can be localized and followed.

In the vicinity of a conical intersection, electronic changes become increasingly rapid as the populations of the two constituting states are switched. The ASRS technique has the temporal resolution for monitoring these changes and detecting the appearance of a CoIn. Moreover, the combination of narrowband and broadband pulses in the Raman probe sequence facilitates unprecedented spectral resolution compared to X-ray absorption. When a CoIn is approached, additional coherence terms emerge from the off-diagonal elements of the density matrix and affect the ASRS signals. ASRS should provide a novel way for the powerful characterization of conical intersections, which are essential to the understanding of ultrafast photo-induced chemical reactions. Due to the high density of states of core excitations, it should deliver clear signatures of CoIn mediated dynamics, even for situations with vanishing energy gaps of valence electronic states which are often hampered by inter valence transition moments and the limited bandwidth of optical probe techniques.[8]

To date, the direct time-resolved experimental probing of conical intersections is rare. Most reported experiments have indirect circumstantial evidence of their presence, by probing the fast dynamics of a vibrational wave packet passing through a conical intersection[8,42] or via the product branching ratio.[43] Ultrafast femtosecond techniques can locate the CoIn with resolution of a few tens of femtoseconds.[44] Recent examples that are sensitive directly to the change in

electronic structure include high harmonic generation study of NO_2,[45] X-ray ionization and fragmentation of hexane,[46] and the Auger probe of thymine.[47] ASRS signals offer a new possibility for capturing signatures of conical intersections. The technique provides a measure for coupled electron nuclear dynamics by mapping the instantaneous occupied valence state on core excitations. The incorporation of dephasing effects due to vibrational motions on different potential energy surfaces will be an important subject for future research. By combining femtosecond-attosecond pump-probe pulses for X-ray Raman detection, broadband signals are recorded in a single shot, making ASRS a promising tool for nonlinear X-ray spectroscopy.

IV. METHODS

A. MD simulation

Trajectories were simulated using the NewtonX 1.2 package[48,49] modified[50] to be compatible with Molpro.[51] The starting points for the individual trajectories were 100 structures taken out of a Wigner phase space distribution along the normal modes of the optimized ground state. Optimization and vibrational frequencies were calculated at the CCSD(T)/6-31G* level. Nonadiabatic dynamics was simulated using the TSH algorithm.[33] No thermostat was used. Energies, gradients, and nonadiabatic couplings were computed every 0.5 fs at the CASSCF/6-31G* level averaged over 4 states. The (10, 9) active space was employed which consists of the entire π-system of furan and both CO-σ bonds and all corresponding antibonding orbitals (supplementary Fig. 14). The nonadiabatic coupling was evaluated only for states closer than 2 eV. Snapshots were then harvested for signal calculations.

B. Transition dipole moments between valence and core states

The MD provided wavefunctions ($|\Psi_n^{MCSCF}\rangle$) and amplitudes (d_n) of 4 valence states ($n = S_0$–S_3) at each geometry. However, the 6-31G* basis set used in these trajectories is not suitable for core hole calculations since it does not adequately describe the short-range asymptotic behavior of the core hole states. We therefore switched to a larger aug-cc-pVDZ basis set.[52] Point test with the aug-cc-pVTZ basis set,[52] verified[36] for well description of the core excited furan, was also performed and similar results were obtained (supplementary Fig. 15). The TDMs between the core and valence states are easier to calculate with the same basis set. We recalculated the valence excited states using the aug-cc-pVDZ basis set, and projected the amplitudes d_n into the new basis set (c_m) (supplementary Note 2). Additional states are needed in order to cover reasonably broad energy range for the ASRS spectroscopy. 10 valence states (V_0–V_9) and 50 core-excited states (C_1–C_{50}) were computed. This provided low-lying valence excited states up till $\sim$10 eV and core states up till the ionic potential (IP). The Molpro package[51] was used for valence and core calculations. The CASSCF method was used for valence calculations. For validation, we calculated the artificial "UV absorption" spectra at different active space sizes. Even though this is not a physical observable at geometries other than **GS**, it provides a good test for the accuracy of the calculated TDMs. Comparison of different active space sizes for selected geometries shows that the active space with 10 orbitals and 10 electrons led to converged spectra (supplementary Figs. 16(a)–16(b)). This active space was used for valence state calculations at all geometries.

MCSCF core state calculations were initiated in the 1980s by Ågren and co-workers.[53–56] In recent years, Odelius *et al.*[57] first employed the state-averaged RASSCF method[37] in conjunction with the state-interaction treatment of SO effects[58] for metal L-edge XANES and RIXS calculations. We started with the optimized 10-state-averaged valence wavefunction and employed RASSCF to calculate the core states. The O1s core orbital was frozen and set with a single occupation (RAS1). For geometries other than **GS** and **Reac-3**, we selected 10 orbitals in the RAS2 space, which allows full configuration interaction (CI). For **GS** and ground-state-like geometry **Reac-3** with mainly closed-shell feature, only 4 orbitals are set in the RAS2 space while 20 more orbitals are included in the RAS3 space with maximum occupation of 1 electron. This gives additional states in the high-energy region, as required for better agreement of the

calculated "O1s XANES spectroscopy" with experiment. Similarly, different active spaces had been tested for selected geometries to verify the accuracy of the calculated TDMs (supplementary Figs. 16(c)–16(d)). The O1s IP was calculated as the difference of the state-specific RASSCF total energies of the ionized and the neutral molecule. Core state energies of **GS** were shifted by -3.05 eV by aligning the first resolved main peak of O1s XANES spectrum to experiment (535.1 eV).[59] The same shift value was then applied for all structures. Additionally, for the ground state geometry, the simulated UV and XANES spectra compare well with experiment[59–62] and theoretical TD-DFT results[36] (supplementary Fig. 17).

We then calculated the TDMs between all valence states m and core states p. The MCSCF wavefunctions are respectively given by $|\Phi_m^{MCSCF}\rangle = \sum_j \lambda_j^m |\phi_j^m\rangle$ and $|\Theta_p^{MCSCF}\rangle = \sum_i \kappa_i^p |\theta_i^e\rangle$, where $|\phi_j^m\rangle$ and $|\theta_i^p\rangle$ are Slater's determinants, λ_j^m and κ_i^e are the CI coefficients. The transition dipole matrix between $|\Phi_m^{MCSCF}\rangle$ and $|\Theta_p^{MCSCF}\rangle$ is given by

$$\langle \Phi_m^{MCSCF} | \hat{\boldsymbol{\mu}} | \Theta_p^{MCSCF} \rangle = \sum_i \sum_j (\lambda_j^m)^* \kappa_i^p \langle \phi_j^m | \hat{\boldsymbol{\mu}} | \theta_i^p \rangle. \tag{4}$$

$\langle \phi_j^m | \hat{\boldsymbol{\mu}} | \theta_i^p \rangle$ were calculated using the Löwdin rules.[63,64]

C. ASRS signal simulations

Using wavefunction and dipole integral matrices, the signals were calculated by our home built code. The two X-ray pulses were X polarized, while the molecule in the initial geometry stays in the XY plane. The narrowband frequency ω_2 was set to 533.0 eV to coincide with the first main peak in the O1s XANES spectra (an average value for all structures). The broadband pulse central frequency ω_3 is set to 5 eV lower, and pulse duration $\sigma = 100$ as. 0.13 eV lifetime broadening was assumed for O1s core excited states.[24] For all valence excited states, a generic value of 0.05 eV was employed.[36,65] For the detection window, ω's from 525 to 540 eV with 0.05 eV intervals were used. Point test was also carried out for **CoIn-3** to examine the effects of pulse (supplementary Fig. 18), where the narrowband frequency ω_2 was tuned from 529.0 eV to 535.0 eV with ω_3 fixed at 528.0 eV.

Our ASRS simulation protocol can be summarized as follows:

1. Nonadiabatic MD simulations at the CASSCF/6-31G* level for 4 valence states (S_0–S_3) generate wavefunctions $|\Psi_n^{MCSCF}\rangle$ and amplitudes d_n; select representative snapshots for consequent steps.
2. CASSCF/aug-cc-pVDZ calculations for 10 valence states (V_0–V_9) to get $|\Phi_m^{MCSCF}\rangle$.
3. RASSCF/aug-cc-pVDZ calculations for 50 core-excited states (C_1–C_{50}) yield the wavefunctions $|\Theta_e^{MCSCF}\rangle$.
4. Project the amplitudes obtained from step 1 (d_n) to the aug-cc-pVDZ level (c_m) according to supplementary Eq. (5).
5. Calculate the TDMs between $|\Phi_m^{MCSCF}\rangle$ and $|\Theta_e^{MCSCF}\rangle$ using Eq. (4).
6. The amplitudes from step 4 and TDMs from step 5 are used to calculate the signals Eqs. (1)–(3).

[1]*Ultrafast Phenomena VII*, edited by C. B. Harris, E. P. Ippen, G. A. Mourou, and A. H. Zewail (Springer-Verlag, Berlin-Heidelberg, 1990).

[2]A. H. Zewail, "Femtochemistry: Atomic-scale dynamics of the chemical bond," J. Phys. Chem. A **104**, 5660–5694 (2000).

[3]A. L. Sobolewski and W. Domcke, "*Ab initio* studies on the photophysics of the guaninevcytosine base pair," Phys. Chem. Chem. Phys. **6**, 2763–2771 (2004).

[4]S. Perun, A. L. Sobolewski, and W. Domcke, "*Ab initio* studies on the radiationless decay mechanisms of the lowest excited singlet states of 9h-adenine," J. Am. Chem. Soc. **127**, 6257–6265 (2005).

[5]C. Z. Bisgaard, O. J. Clarkin, G. Wu, A. M. D. Lee, O. Geßner, C. C. Hayden, and A. Stolow, "Time-resolved molecular frame dynamics of fixed-in-space CS2 molecules," Science **323**, 1464–1468 (2009).

[6]K. Haiser, B. P. Fingerhut, K. Heil, A. Glas, T. T. Herzog, B. M. Pilles, W. J. Schreier, W. Zinth, R. de Vivie-Riedle, and T. Carell, "Mechanism of UV-Induced Formation of Dewar Lesions in DNA," Angew. Chem. Int. Ed. **51**, 408–411 (2012).

[7]L. M. Frutos, T. Andruniów, F. Santoro, N. Ferré, and M. Olivucci, "Tracking the excited-state time evolution of the visual pigment with multiconfigurational quantum chemistry," Proc. Natl. Acad. Sci. **104**, 7764–7769 (2007).

[8]D. Polli, P. Altoè, O. Weingart, K. M. Spillane, C. Manzoni, D. Brida, G. Tomasello, G. Orlandi, P. Kukura, R. A. Mathies, M. Garavelli, and G. Cerullo, "Conical intersection dynamics of the primary photoisomerization event in vision," Nature **467**, 440–443 (2010).

[9]G. Tomasello, M. J. Bearpark, M. A. Robb, G. Orlandi, and M. Garavelli, "Significance of a zwitterionic state for fulgide photochromism: Implications for the design of mimics," Angew. Chem. Int. Ed. **49**, 2913–2916 (2010).

[10]A. Hofmann and R. de Vivie-Riedle, "Adiabatic approach for ultrafast quantum dynamics mediated by simultaneously active conical intersections," Chem. Phys. Lett. **346**, 299–304 (2001).

[11]A. M. Müller, S. Lochbrunner, W. E. Schmid, and W. Fuß, "Low-Temperature Photochemistry of Previtamin D: A Hula-Twist Isomerization of a Triene," Angew. Chem. Int. Ed. **37**, 505–507 (1998).

[12]B. C. Arruda and R. J. Sension, "Ultrafast polyene dynamics: The ring opening of 1,3-cyclohexadiene derivatives," Phys. Chem. Chem. Phys. **16**, 4439–4455 (2014).

[13]B. P. Fingerhut, C. F. Sailer, J. Ammer, E. Riedle, and R. de Vivie-Riedle, "Buildup and decay of the optical absorption in the ultrafast photo-generation and reaction of benzhydryl cations in solution," J. Phys. Chem. A **116**, 11064–11074 (2012).

[14]M. Lipson, A. A. Deniz, and K. S. Peters, "The sub-picosecond dynamics of diphenylmethylchloride ion pairs and radical pairs," Chem. Phys. Lett. **288**, 781–784 (1998).

[15]L. Blancafort, F. Jolibois, M. Olivucci, and M. A. Robb, "Potential energy surface crossings and the mechanistic spectrum for intramolecular electron transfer in organic radical cations," J. Am. Chem. Soc. **123**, 722–732 (2001).

[16]*Conical Intersections: Electronic Structure, Dynamics & Spectroscopy*, edited by W. Domcke, D. R. Yarkony, and H. Köppel (World Scientific, Singapore, 2004).

[17]P. von den Hoff, R. Siemering, M. Kowalewski, and R. de Vivie-Riedle, "Electron dynamics and its control in molecules: From diatomics to larger molecular systems," IEEE J. Sel. Top. Quantum Electron. **18**, 119–129 (2012).

[18]J. Krause, K. Schafer, and K. Kulander, "High-order harmonic generation from atoms and ions in the high intensity regime," Phys. Rev. Lett. **68**, 3535–3538 (1992).

[19]P. Corkum, "Plasma perspective on strong field multiphoton ionization," Phys. Rev. Lett. **71**, 1994–1997 (1993).

[20]H. Kapteyn, O. Cohen, I. Christov, and M. Murnane, "Harnessing attosecond science in the quest for coherent x-rays," Science **317**, 775–778 (2007).

[21]K. T. Kim, D. M. Villeneuve, and P. B. Corkum, "Manipulating quantum paths for novel attosecond measurement methods," Nat. Photonics **8**, 187–194 (2014).

[22]P. Emma, R. Akre, J. Arthur, R. Bionta, C. Bostedt, J. Bozek, A. Brachmann, P. Bucksbaum, R. Coffee, F.-J. Decker, Y. Ding, D. Dowell, S. Edstrom, A. Fisher, J. Frisch, S. Gilevich, J. Hastings, G. Hays, P. Hering, Z. Huang, R. Iverson, H. Loos, M. Messerschmidt, A. Miahnahri, S. Moeller, H.-D. Nuhn, G. Pile, D. Ratner, J. Rzepiela, D. Schultz, T. Smith, P. Stefan, H. Tompkins, J. Turner, J. Welch, W. White, J. Wu, G. Yocky, and J. Galayda, "First lasing and operation of an ångstrom-wavelength free-electron laser," Nat. Photonics. **4**, 641–647 (2010).

[23]J. Ullrich, A. Rudenko, and R. Moshammer, "Free-electron lasers: New avenues in molecular physics and photochemistry," Annu. Rev. Phys. Chem. **63**, 635–660 (2012).

[24]G. H. Zschornack, *Handbook of X-Ray Data*, 1st ed. (Springer, Berlin, 2007).

[25]P. Kukura, D. W. McCamant, and R. A. Mathies, "Femtosecond stimulated Raman spectroscopy," Annu. Rev. Phys. Chem. **58**, 461–488 (2007).

[26]K. E. Dorfman, B. P. Fingerhut, and S. Mukamel, "Time-resolved broadband raman spectroscopies: A unified six-wave-mixing representation," J. Chem. Phys. **139**, 124113 (2013).

[27]K. E. Dorfman, B. P. Fingerhut, and S. Mukamel, "Broadband infrared and Raman probes of excited-state vibrational molecular dynamics: simulation protocols based on loop diagrams," Phys. Chem. Chem. Phys. **15**, 12348–12359 (2013).

[28]Y. Zhang, J. D. Biggs, W. Hua, S. Mukamel, and K. E. Dorfman, "Three-dimensional attosecond resonant stimulated x-ray raman spectroscopy of electronic excitations in core-ionized glycine," Phys. Chem. Chem. Phys. **16**, 24323 (2014).

[29]M. Tashiro, M. Ehara, H. Fukuzawa, K. Ueda, C. Buth, N. V. Kryzhevoi, and L. S. Cederbaum, "Molecular double core hole electron spectroscopy for chemical analysis," J. Chem. Phys. **132**, 184302 (2010).

[30]H. Nakamura, *Nonadiabatic Transition: Concepts, Basic Theories and Applications* (World Scientific, 2012).

[31]See supplementary material at http://dx.doi.org/10.1063/1.4933007 for supplementary Figs. 1–18, Table 1, and Notes 1–2.

[32]D. R. Yarkony, "Nonadiabatic quantum chemistrypast, present, and future," Chem. Rev. **112**, 481–498 (2011).

[33]J. C. Tully, "Molecular dynamics with electronic transitions," J. Chem. Phys. **93**, 1061–1071 (1990).

[34]N. Gavrilov, S. Salzmann, and C. M. Marian, "Deactivation via ring opening: A quantum chemical study of the excited states of furan and comparison to thiophene," Chem. Phys. **349**, 269–277 (2008).

[35]T. Fuji, Y.-I. Suzuki, T. Horio, T. Suzuki, R. Mitrić, U. Werner, and V. Bonačić-Koutecký, "Ultrafast photodynamics of furan," J. Chem. Phys. **133**, 234303–234303–9 (2010).

[36]W. Hua, J. D. Biggs, Y. Zhang, D. Healion, H. Ren, and S. Mukamel, "Multiple core and vibronic coupling effects in attosecond stimulated x-ray raman spectroscopy," J. Chem. Theory Comput. **9**, 5479–5489 (2013).

[37]P. Å. Malmqvist, A. Rendell, and B. O. Roos, "The restricted active space self-consistent-field method, implemented with a split graph unitary group approach," J. Phys. Chem. **94**, 5477–5482 (1990).

[38]R. Martin, "Natural transition orbitals," J. Chem. Phys. **118**, 4775 (2003).

[39]I. Mayer, "Identifying a pair of interacting chromophores by using SVD transformed CIS wave functions," Chem. Phys. Lett. **443**, 420–425 (2007).

[40]P. Å. Malmqvist and V. Veryazov, "The binatural orbitals of electronic transitions," Mol. Phys. **110**, 2455–2464 (2012).

[41]M. Alagia, M. Lavollée, R. Richter, U. Ekström, V. Carravetta, D. Stranges, B. Brunetti, and S. Stranges, "Probing the potential energy surface by high-resolution x-ray absorption spectroscopy: The umbrella motion of the core-excited CH3 free radical," Phys. Rev. A **76**, 022509 (2007).

[42]T. A. A. Oliver, N. H. C. Lewis, and G. R. Fleming, "Correlating the motion of electrons and nuclei with two-dimensional electronic vibrational spectroscopy," Proc. Natl. Acad. Sci. U.S.A. **111**, 10061–10066 (2014).

[43]J. S. Lim and S. K. Kim, "Experimental probing of conical intersection dynamics in the photodissociation of thioanisole," Nat. Chem. **2**, 627–632 (2010).

[44]T. Horio, T. Fuji, Y.-I. Suzuki, and T. Suzuki, "Probing ultrafast internal conversion through conical intersection via time-energy map of photoelectron angular anisotropy," J. Am. Chem. Soc. **131**, 10392–10393 (2009).

[45]H. J. Wörner, J. B. Bertrand, B. Fabre, J. Higuet, H. Ruf, A. Dubrouil, S. Patchkovskii, M. Spanner, Y. Mairesse, V. Blanchet, E. Mvel, E. Constant, P. B. Corkum, and D. M. Villeneuve, "Conical intersection dynamics in NO2 probed by homodyne high-harmonic spectroscopy," Science **334**, 208–212 (2011).

[46]V. S. Petrović, M. Siano, J. L. White, N. Berrah, C. Bostedt, J. D. Bozek, D. Broege, M. Chalfin, R. N. Coffee, J. Cryan, L. Fang, J. P. Farrell, L. J. Frasinski, J. M. Glownia, M. Gühr, M. Hoener, D. M. P. Holland, J. Kim, J. P. Marangos, T. Martinez, B. K. McFarland, R. S. Minns, S. Miyabe, S. Schorb, R. J. Sension, L. S. Spector, R. Squibb, H. Tao, J. G. Underwood, and P. H. Bucksbaum, "Transient x-ray fragmentation: Probing a prototypical photoinduced ring opening," Phys. Rev. Lett. **108**, 253006 (2012).

[47]B. K. McFarland, J. P. Farrell, S. Miyabe, F. Tarantelli, A. Aguilar, N. Berrah, C. Bostedt, J. D. Bozek, P. H. Bucksbaum, J. C. Castagna, R. N. Coffee, J. P. Cryan, L. Fang, R. Feifel, K. J. Gaffney, J. M. Glownia, T. J. Martinez, M. Mucke, B. Murphy, A. Natan, T. Osipov, V. S. Petrovió, S. Schorb, T. Schultz, L. S. Spector, M. Swiggers, I. Tenney, S. Wang, J. L. White, W. White, and M. Gühr, "Ultrafast x-ray auger probing of photoexcited molecular dynamics," Nat. Commun. **5**, 4235 (2014).

[48]M. Barbatti, G. Granucci, M. Ruckenbauer, F. Plasser, J. Pittner, M. Persico, and H. Lischka, "NEWTON-X: A package for Newtonian dynamics close to the crossing seam," version 1.2, www.newtonx.org (2011).

[49]M. Barbatti, G. Granucci, M. Persico, M. Ruckenbauer, M. Vazdar, M. Eckert-Maksiá, and H. Lischka, "The on-the-fly surface-hopping program system newton-x: Application to *ab initio* simulation of the nonadiabatic photodynamics of benchmark systems," J. Photochem. Photobiol. A **190**, 228–240 (2007).

[50]B. P. Fingerhut, S. Oesterling, K. Haiser, K. Heil, A. Glas, W. J. Schreier, W. Zinth, T. Carell, and R. de Vivie-Riedle, "Oniom approach for non-adiabatic on-the-fly molecular dynamics demonstrated for the backbone controlled dewar valence isomerization," J. Chem. Phys. **136**, 204307 (2012).

[51]H.-J. Werner, P. J. Knowles, G. Knizia, F. R. Manby, M. Schütz, P. Celani, T. Korona, R. Lindh, A. Mitrushenkov, G. Rauhut, K. R. Shamasundar, T. B. Adler, R. D. Amos, A. Bernhardsson, A. Berning, D. L. Cooper, M. J. O. Deegan, A. J. Dobbyn, F. Eckert, E. Goll, C. Hampel, A. Hesselmann, G. Hetzer, T. Hrenar, G. Jansen, C. Köppl, Y. Liu, A. W. Lloyd, R. A. Mata, A. J. May, S. J. McNicholas, W. Meyer, M. E. Mura, A. Nicklass, D. P. O'Neill, P. Palmieri, D. Peng, K. Pflüger, R. Pitzer, M. Reiher, T. Shiozaki, H. Stoll, A. J. Stone, R. Tarroni, T. Thorsteinsson, and M. Wang, MOLPRO, version 2012.1, a package of *ab initio* programs (2012).

[52]T. H. Dunning, "Gaussian basis sets for use in correlated molecular calculations. I. The atoms boron through neon and hydrogen," J. Chem. Phys. **90**, 1007–1023 (1989).

[53]H. J. A. Jensen, P. Jørgensen, and H. Ågren, "Efficient optimization of large scale MCSCF wave functions with a restricted step algorithm," J. Chem. Phys. **87**, 451–466 (1987).

[54]H. Ågren and H. J. Å. Jensen, "An efficient method for the calculation of generalized overlap amplitudes for core photo-electron shake-up spectra," Chem. Phys. Lett. **137**, 431–436 (1987).

[55]H. Ågren, A. Flores-Riveros, and H. J. Å. Jensen, "An efficient method for calculating molecular radiative intensities in the VUV and soft x-ray wavelength regions," Phys. Scr. **40**, 745 (1989).

[56]H. Ågren and H. J. Å. Jensen, "Relaxation and correlation contributions to molecular double core ionization energies," Chem. Phys. **172**, 45–57 (1993).

[57]I. Josefsson, K. Kunnus, S. Schreck, A. Föhlisch, F. de Groot, P. Wernet, and M. Odelius, "*Ab initio* calculations of x-ray spectra: Atomic multiplet and molecular orbital effects in a multiconfigurational SCF approach to the l-edge spectra of transition metal complexes," J. Phys. Chem. Lett. **3**, 3565–3570 (2012).

[58]P. A. Malmqvist, B. O. Roos, and B. Schimmelpfennig, "The restricted active space (RAS) state interaction approach with spin-orbit coupling," Chem. Phys. Lett. **357**, 230–240 (2002).

[59]D. Duflot, J.-P. Flament, A. Giuliani, J. Heinesch, and M.-J. Hubin-Franskin, "Core shell excitation of furan at the O1*s* and C1*s* edges: An experimental and *ab initio* study," J. Chem. Phys. **119**, 8946–8955 (2003).

[60]M. H. Palmer, I. C. Walker, C. C. Ballard, and M. F. Guest, "The electronic states of furan studied by VUV absorption, near-threshold electron energy-loss spectroscopy and *ab initio* multi-reference configuration interaction calculations," Chem. Phys. **192**, 111–125 (1995).

[61]D. C. Newbury, I. Ishii, and A. P. Hitchcock, "Inner shell electron-energy loss spectroscopy of some heterocyclic molecules," Can. J. Chem. **64**, 1145–1155 (1986).

[62]Z. D. Pešić, D. Rolles, I. Dumitriu, and N. Berrah, "Fragmentation dynamics of gas-phase furan following *K*-shell ionization," Phys. Rev. A **82**, 013401 (2010).

[63]P.-O. Löwdin, "Quantum theory of many-particle systems. I. Physical interpretations by means of density matrices, natural spin-orbitals, and convergence problems in the method of configurational interaction," Phys. Rev. **97**, 1474–1489 (1955).

[64]D. B. Cook, *Handbook of Computational Quantum Chemistry* (Dover Publications, Mineola, NY, 2005), pp. 66–69.

[65]D. Healion, H. Wang, and S. Mukamel, "Simulation and visualization of attosecond stimulated x-ray Raman spectroscopy signals in *trans*-N-methylacetamide at the nitrogen and oxygen K-edges," J. Chem. Phys. **134**, 124101 (2011).

[66]J. D. Biggs, J. A. Voll, and S. Mukamel, "Coherent nonlinear optical studies of elementary processes in biological complexes: diagrammatic techniques based on the wave function versus the density matrix," Philos. Trans. R. Soc. A **370**, 3709–3727 (2012).